
TrajTok: Adaptive Spatial Tokenization for Trajectory Representation Learning

Zhen Xiong

University of Southern California
z.xiong@usc.edu

Shang-Ling Hsu

University of Southern California
hsushang@usc.edu

Cyrus Shahabi

University of Southern California
shahabi@usc.edu

Abstract

Learning generalizable trajectory representations from raw GPS traces remains difficult because the data is continuous, noisy, irregularly sampled. Even the choice of spatial tokenization is challenging: many existing approaches rely on fixed-size grids, but fine-resolution grids often produce cells with too few GPS visits to learn robust embeddings, while coarse-resolution grids suffer from internal fragmentation, merging heterogeneous local movement patterns into the same token. We present TrajTok, a trajectory encoder with simple pretraining recipe that produce highly generalizable trajectory embeddings for diverse downstream applications. First, we train a tokenizer that learns a multi-resolution hexagonal cell partition from the spatial distribution of GPS points, mapping a continuous, noisy GPS sequence into a discrete series of cells as *tokens*. Then, to capture both the geometric and kinematic features of trajectories, we introduce a factorized transformer encoder architecture with early per-modality self-attention blocks followed by cross-attention fusion layers. We further incorporate spatiotemporal rotary position embeddings (ST-RoPE) to encode where and when each token occurs along the trajectory. We pretrain TrajTok with a simple yet effective masked token modeling objective that encourages the model to recover both geometric structure and kinematics patterns from partial trajectory observations, leading to representations that can actually transfer effectively across diverse downstream tasks. Empirically, our pretrained *frozen* TrajTok encoder with lightweight task adapters reaches 0.435 HR@1 on trajectory similarity search, 0.773 macro-F1 on classification, 42.27 s MAE on Estimated time of arrival (ETA), and 38.41 s MAE on full travel-time regression on Porto dataset, outperforming multiple state-of-the-art task-specific methods. Notably, the *same frozen* encoder handles both geometry-dominated tasks (e.g., similarity search) and kinematics-dominated tasks (e.g., travel-time estimation), indicating that the learned representation captures transferable structure rather than task-specific shortcuts. This suggests that our learned multi-resolution spatial tokenization, combined with simple masked-token pretraining, is a promising framework for general-purpose trajectory foundation models.

1 Introduction

The analysis of human mobility has become a cornerstone of modern spatial computing, driving advancements in urban planning [32], epidemic control [1], and intelligent transportation systems

[25]. At the core of these applications lies the need to effectively model and understand GPS trajectories—sequences of geospatial coordinates that capture the continuous movement of entities over time.

Despite the proliferation of massive spatial datasets, learning robust, generalized representations of GPS trajectories remains a formidable challenge. Raw trajectory data is inherently noisy, irregularly sampled, and strictly constrained by underlying road networks and map topologies. Existing foundation models for trajectory intelligence [19, 33] and geographic representation learning paradigms, such as Space2Vec [18], often rely on rigid, grid-based spatial discretization. These conventional methods struggle to preserve fine-grained spatio-temporal dynamics and fail to account for the complex structural constraints imposed by real-world environments.

To bridge this gap, we introduce TrajTok, a novel framework for learning geospatial representations of GPS trajectories via adaptive tokenization. Unlike traditional fixed-grid segmentation, our adaptive tokenization strategy partitions continuous trajectories into dynamical spatial tokens. Furthermore, to learn generalizable trajectory representations, TrajTok factorize geometric and kinematics features learning process at early stage using self-attention and then fuse them later via cross-attention mechanism.

To pretrain TrajTok, we adopt a simple factorized masked objective tailored to raw GPS token sequence. Given a partially masked trajectory, the geometric channel predicts the masked spatial cell IDs, while the kinematic channel reconstructs the corresponding motion targets, namely normalized speed and heading. Combined with density-adaptive tokenization, factorized geometric and kinematic representations, and cross-attention fusion with spatiotemporal positional encoding, this objective encourages the model to capture both route geometry and motion dynamics directly from noisy, irregularly sampled GPS traces. We evaluate the resulting pretrained encoder on four Porto benchmarks spanning both geometry-dominated and kinematics-dominated transfer: trajectory similarity search, call-type classification, prefix-based ETA prediction, and full-trajectory travel-time regression. Across all four tasks, a single frozen TrajTok encoder with lightweight task heads matches or outperforms strong prior task-specific methods, indicating that the learned representation captures transferable trajectory structure rather than task-specific shortcuts.

Our main contributions are summarized as follows:

- We propose TrajTok, a trajectory representation framework that converts raw GPS trajectories into multi-resolution spatial tokens through a density-adaptive tokenization, allocating finer cells to dense regions while preserving a compact vocabulary.
- We introduce a factorized transformer encoder that separates geometric location signals from kinematic motion signals in early layers, then fuses them through cross-attention to form a unified trajectory representation.
- We develop a simple and effective pretraining recipe based on co-masked spatial token prediction and kinematic regression, together with run-aware span masking designed for raw token streams with repeated-cell runs.
- We show that the same frozen pretrained encoder transfers strongly across similarity retrieval, classification, estimated time of arrival (ETA) regression, demonstrating robust performance across both geometric and motion-sensitive downstream tasks.

2 Related Work

Some neural approaches to trajectory representation learning operate directly on raw coordinate sequences or point-level GPS features [24, 27]. Spatial discretization, however, remains widely used because it converts continuous, noisy GPS traces into reusable symbolic units amenable to embedding, reconstruction, masking, or contrast — instantiated in prior work as fixed grids, geohashes, road segments, or learned regions [13, 30, 5, 2, 14, 19]. Yet because mobility data is strongly non-uniform, any fixed granularity faces an inherent tradeoff: fine cells preserve detail in dense areas but fragment sparse ones, while coarse cells offer stronger statistical support at the cost of merging heterogeneous patterns. This tension motivates adaptive tokenization, where spatial resolution is allocated according to the empirical density of trajectory observations.

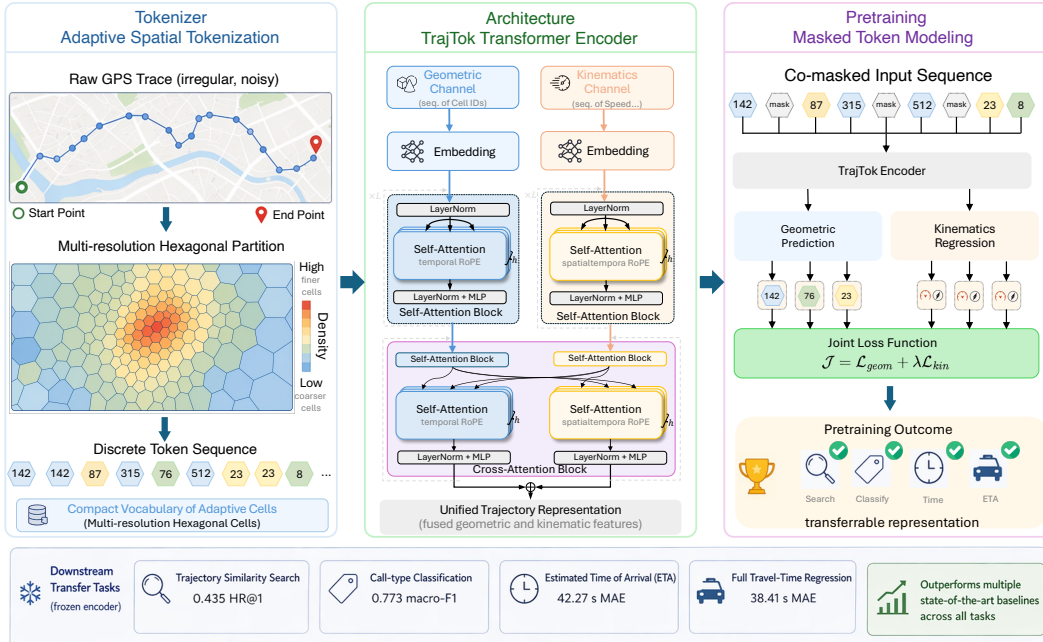


Figure 1: Overview of **TrajTok**. **(Left)** *Adaptive spatial tokenization*: raw, irregular GPS trajectories are partitioned using a density-adaptive multi-resolution hexagonal grid, producing a compact vocabulary of spatial cells and a discrete token sequence. **(Middle)** *Factorized transformer encoder*: tokens are represented through two streams—a geometric channel (cell IDs) and a kinematic channel (motion features such as speed and heading)—processed by separate self-attention blocks with spatiotemporal RoPE and fused via cross-attention to form a unified trajectory representation. **(Right)** *Pretraining via co-masked token modeling*: masked positions are shared across channels, while geometric cell prediction and kinematic regression are optimized in parallel under a joint objective. The resulting pretrained encoder learns transferable representations that generalize across diverse downstream tasks.

A complementary line of work imposes stronger geographic structure through map matching and road-network modeling, representing trajectories as road-segment sequences and combining graph-based road encoders with transformer pretraining [11, 16, 20]. These approaches can be effective when accurate road graphs and matching pipelines are available, but rely on preprocessing assumptions that TrajTok deliberately avoids, operating instead on raw GPS trajectories after density-adaptive spatial tokenization.

Trajectory similarity learning has been a central evaluation protocol for the field, with methods such as t2vec [13], NeuTraj [30], TrajCL [2], and SIMformer [27] defining strong baselines. At the same time, regression and classification tasks such as travel-time estimation and trip labeling provide complementary tests of whether a learned representation transfers beyond geometric similarity [11, 20].

3 Methodology

In this section, we describe the tokenization pipeline, the factorized encoder, and the masked pretraining objectives used by the current TrajTok implementation. See Figure 1 as the overview.

3.1 Problem Formulation

A raw GPS trajectory $\mathcal{T} = \{p_1, p_2, \dots, p_n\}$ is a chronologically ordered sequence of points, where $p_i = (\phi_i, \lambda_i, t_i)$ contains latitude ϕ_i , longitude λ_i , and timestamp t_i . Our goal is to learn an encoder $f_\theta(\mathcal{T})$ that produces contextual token states and a transferable trajectory representation suitable for

both structure-oriented tasks such as similarity search and motion-sensitive tasks such as travel-time prediction.

3.2 Adaptive Spatial Tokenization

Learning Density-adaptive vocabulary. We build the token vocabulary with the hierarchical H3 hexagonal grid [22]. Starting from a base resolution r_{base} , we count training points inside each cell. Cells whose counts exceed a capacity threshold are split into their children, and the process repeats until the count falls below the threshold or the maximum resolution r_{max} is reached. The resulting vocabulary contains cells at multiple resolutions and allocates finer spatial units to high-density regions. See Algorithm 1 for more details.

Trajectory-to-tokens conversion. Each GPS point is mapped to the highest-resolution vocabulary cell that contains it. A token therefore carries a discrete cell ID, the cell resolution, the original coordinates, and the timestamp.

3.3 Factorized Token Representation

We represent each token along two factorized channels: a *geometric* channel encoding where the token lies in space, and a *kinematic* channel encoding how the agent is moving at that token. These two channels are processed by separate streams in the encoder (§3.4) and recombined through cross-attention fusion, allowing the model to specialize before unifying.

Geometric channel. The geometric embedding is a learned cell-identity vector,

$$\mathbf{g}_j = \mathbf{e}_{c_j}, \quad (1)$$

where \mathbf{e}_{c_j} is the embedding of the token’s corresponding spatial cell.

Kinematic channel. The kinematic embedding captures per-token speed and heading. Rather than discretizing these quantities into bins, we represent them continuously and encode heading through its sine and cosine to respect its circular structure:

$$\mathbf{x}_j^{\text{kin}} = \left[\frac{v_j}{v_{\text{max}}}, \sin \theta_j, \cos \theta_j \right], \quad \mathbf{k}_j = \text{MLP}(\mathbf{x}_j^{\text{kin}}). \quad (2)$$

Here v_j is the haversine-distance-over-time speed between consecutive tokens. θ_j is the corresponding bearing; and the MLP is two-layer with GeGLU activation.

3.4 Spatiotemporal RoPE

The encoder contains a geometric channel and a kinematic channel. Each channel first passes through independent embedding layer and then RoPE-equipped self-attention layers, after which paired fusion layers apply self-attention followed by cross-attention between channels.

Geometric positional encoding. The geometric channel uses **Spatial-Temporal Rotary Position Embeddings** [21] (ST-RoPE) over latitude, longitude, and time. Coordinates and timestamps are normalized relative to the trajectory start.

Kinematic positional encoding. The kinematic channel uses temporal-only RoPE, since speed and heading evolve primarily as functions of time.

Cross-attention fusion. In a fusion block, each stream updates itself with commonly used self-attention and then attends to the other channel with cross-attention. For mathematical formulation of the self/cross-attention we used, see Appendix B.3 for details.

3.5 Factorized Masked Pretraining

Co-masked cell prediction. Given a mask set \mathcal{M} , the geometric stream predicts the original cell IDs at masked positions:

$$\mathcal{L}_{\text{geom}} = -\frac{1}{|\mathcal{M}|} \sum_{j \in \mathcal{M}} \log p_{\theta}(c_j | \mathbf{G}). \quad (3)$$

Co-masked kinematic regression. At the same masked positions, the kinematic stream reconstructs normalized speed and heading targets:

$$\mathcal{L}_{\text{kin}} = \beta_{\text{speed}} \text{MSE}(\hat{v}_j, v_j/v_{\text{max}}) + \frac{1}{2} \beta_{\text{heading}} \text{MSE}(\widehat{\sin \theta}_j, \sin \theta_j) + \frac{1}{2} \beta_{\text{heading}} \text{MSE}(\widehat{\cos \theta}_j, \cos \theta_j) \quad (4)$$

Joint objective. The default joint pretraining objective we use is the linear combination of previous two loss functions:

$$\mathcal{J} = \mathcal{L}_{\text{geom}} + \lambda \mathcal{L}_{\text{kin}}. \quad (5)$$

We use *run-aware* span masking that rejects candidate spans lying entirely inside a single repeated-cell run; see Appendix C.1 for details and a comparison to naive masking.

4 Experiments

We evaluate a single frozen TrajTok encoder across four trajectory-related tasks spanning two regimes: geometry-dominated (§4.2: trajectory similarity search, §4.3: call-type classification) and kinematics-dominated (§4.4: ETA from prefixes, §4.5: full-trajectory travel-time regression). With only lightweight task adapters, our frozen pretrained encoder matches or outperforms task-specific baselines across all four benchmarks (Tables 1–4). Controlled ablations (§4.6) further isolate three drivers of this transfer: density-adaptive tokenization, cross-attention fusion between factorized channels, and pretraining recipe.

4.1 Experimental Setup

For dataset statistics, tokenization configuration, spatial vocabulary and model hyperparameters, see Appendix B.1 for detailed description.

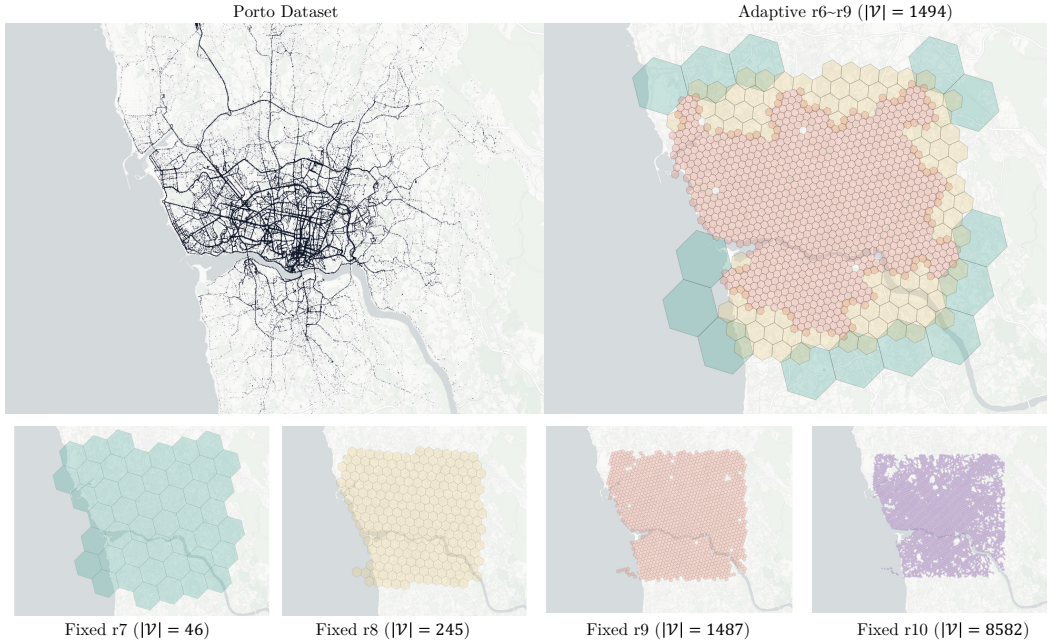


Figure 2: Fixed vs. adaptive spatial tokenization on Porto. Top: raw data (left) and adaptive partition (right; $r6-r9$, $|\mathcal{V}| = 1494$), where cell density follows data distribution. Bottom: fixed hex grids using different resolutions. Adaptive tokenization better balances resolution and vocabulary by refining dense regions and coarsening sparse areas.

Table 1: Trajectory similarity search on Porto. Both TrajTok rows share a common retrieval bank and DTW ground truth. Best results in **bold**; Second best are underlined.

Method	HR@1 \uparrow	R5@20 \uparrow	MRR \uparrow	NDCG@50 \uparrow
t2vec [13]	0.239	0.624	0.373	0.490
CL-TSim [5]	0.116	0.362	0.204	0.266
NeuTraj [30]	0.308	0.807	0.448	0.672
TrajCL [2]	0.217	0.603	0.343	0.556
TrajGAT [31]	0.296	0.683	0.437	0.450
KGTS [4]	0.253	0.444	0.369	0.411
SIMformer [27]	0.300	0.755	0.446	0.651
Space2Vec [17]	0.260	0.879	0.380	0.291
SatClip [12]	0.177	0.907	0.300	0.406
TrajTok (zero-shot)	<u>0.351</u>	<u>0.964</u>	<u>0.503</u>	0.528
TrajTok (retrieval head)	0.435	0.983	0.588	<u>0.661</u>

4.2 Trajectory Similarity Search

We construct a DTW¹-labeled retrieval bank from the held-out test split: 1,000 queries against a fixed 10,000-trajectory corpus, with ground-truth relevance defined by DTW distance on raw GPS sequences. Top- k Hit Ratio (HR@ k) and Mean Reciprocal Rank (MRR) evaluate whether the embedding-based ranking retrieves the DTW-nearest trajectory, treating the single exact-DTW nearest neighbor as the primary positive; top- k Partial Hit Ratio ($R_m@k$) and Normalized Discounted Cumulative Gain (NDCG) further evaluate how well the retrieved ranking preserves the top exact-similarity neighbors [15]. Ranking is by cosine similarity of L2-normalized embeddings. Ranking is by cosine similarity of L2-normalized embeddings. Our retrieval head is finetuned with mixed InfoNCE and rank distillation; see Appendix B.2 for the full configuration.

Results. Table 1 reports both a zero-shot variant (mean-pooled frozen encoder output) and the attentive retrieval head. With the retrieval head, TrajTok attains the best HR@1 (0.435), R5@20 (0.983), and MRR (0.588), improving over the strongest prior baseline by 0.127, 0.176, and 0.140 respectively. On NDCG@50, TrajTok ranks second to NeuTraj (0.658 vs. 0.672); we note that our retrieval head’s training criterion (Appendix B.2) emphasizes top-of-list correctness over the broader top-50 ordering that NDCG@50 rewards. Additionally, our zero-shot variant alone already surpasses all prior methods on HR@1 and R5@20, indicating that the pretrained representation captures DTW-aligned geometric structure without any retrieval-specific finetuning.

4.3 Trajectory Classification

We predict Porto *call type* (different labels indicating how the taxi trip was requested). The classifier freezes the encoder and trains a head that concatenates attentive-pooled trajectory features with a compact departure-context information; see Appendix B.2 for adapter and optimization details.

Results. Table 2 shows that TrajTok attains the best macro-F1 (0.773) and the second-best micro-F1 (0.811), within 0.002 of START (0.813 / 0.772). We do not claim a decisive numerical advantage on this benchmark in isolation; the relevant comparison is qualitative. START relies on map-matched road segments and a dedicated road-network encoder, and JGRM (0.805 / 0.768) jointly models GPS points and routes — both incorporate stronger geographic inductive biases than TrajTok, which operates only on raw GPS streams. Matching these specialized pipelines with a single *frozen* encoder and a lightweight head supports our claim that the learned representation captures transferable trajectory structure rather than task-specific shortcuts. Because call type is a geometry-dominated label, this result primarily exercises the effectiveness of our geometric channel.

4.4 Estimated Time of Arrival (ETA) from Prefixes

ETA is our primary kinematic transfer test. Given an observed *prefix* of a trip and a known destination, the model predicts the remaining travel time. The frozen encoder consumes the prefix trajectory,

¹Dynamic Time Warping (DTW) is an algorithm for measuring similarity between two temporal sequences

Table 2: Porto call-type classification. Best results in **bold**; Second best are underlined.

Method	Micro-F1 \uparrow	Macro-F1 \uparrow
Traj2vec [29]	0.515	0.323
TrajCL [2]	0.801	0.761
PIM [28]	0.728	0.613
START [11]	0.813	<u>0.772</u>
JGRM [16]	0.805	<u>0.768</u>
TrajTok (ours)	<u>0.811</u>	0.773

Table 3: Estimated Time of Arrival on Porto. **Bold** marks the best reported value.

Method	MAPE (%) \downarrow	MAE (s) \downarrow	RMSE (s) \downarrow
DeepTTE [24]	19.65	119.52	183.59
CompactETA [10]	19.37	115.82	174.25
ConSTGAT [7]	18.68	109.79	168.39
TransferTTE [6]	18.61	109.56	168.17
MAML [9]	17.80	102.02	158.76
SSML [8]	17.68	98.63	150.96
MetaER-TTE [6]	17.37	93.75	145.39
TrajTok (ours)	12.42	42.27	72.05

and a destination-conditioned adapter predicts the remaining travel time under a randomized-prefix training regime; full adapter configuration is in Appendix B.2.

Results. Table 3 shows that TrajTok achieves **42.27 s** MAE on randomized-prefix ETA, substantially below the reported Porto MAE range of prior neural travel-time systems. This result is notable because TrajTok uses a single frozen representation shared across downstream tasks, with no task-specific trajectory encoder and no manual feature engineering.

4.5 Full-Trajectory Travel-Time Regression

As a complementary kinematic benchmark, we predict total travel time from the entire observed trip. We acknowledge that total travel time admits a strong correlation with observed sequence length, which makes this task substantially easier than prefix-based ETA.

Results. Table 4 reports total travel-time MAE from the full observed trajectory. This is a strict subcase of ETA at prefix=100% and admits a strong length correlation, so it is a weaker test than §4.4. Nonetheless, TrajTok still attains 38.4 s MAE, a substantial gap to prior work.

Table 4: Full-trajectory travel-time regression on Porto. See §4.5 for protocol caveat.

Method	MAE (s) \downarrow	MAPE (%) \downarrow	RMSE (s) \downarrow
t2vec [13]	115.27	17.68	172.83
CL-TSim [5]	162.62	25.30	241.67
TrajCL [2]	97.42	14.38	154.32
CSTTE [14]	113.29	17.04	175.52
START [11]	131.40	19.94	196.71
TIGR [20]	86.86	12.76	139.80
TrajTok (ours)	38.41	5.71	65.90

4.6 Ablation Studies

We ablate TrajTok along three axes corresponding to our three core design choices: density-adaptive tokenization (§4.6.1), cross-attention fusion between factorized channels (§4.6.2), and the pretraining recipe (§4.6.3). Each ablation isolates a single design decision while holding all other components fixed. Additional controls, including masking-strategy variants and deduplication compression, are discussed and reported in Appendix C.

4.6.1 Density-Adaptive Tokenization

We first study whether adaptive tokenization is necessary or if a well-chosen fixed resolution suffices. Table 5 compares our density-adaptive vocabulary against fixed resolutions from 7 to 10 (see Figure 2 for visualization), with all other components held constant.

Table 5: Tokenizer ablation: density-adaptive vs. fixed-resolution H3. All configurations use the same factorized encoder, factorized masked objective, and 12k training steps. Retrieval metrics come from zero-shot DTW similarity search on a 1k query \times 10k corpus Porto bank (frozen encoder, no finetuning). Best results in **bold**.

Tokenizer	Vocab size	Val loss \downarrow	HR@1 \uparrow	MRR \uparrow	NDCG@5 \uparrow	Spearman \uparrow
r7 (<i>fixed</i>)	46	0.143 [†]	0.197	0.314	0.296	0.263
r8 (<i>fixed</i>)	245	0.330	0.275	0.421	0.443	0.470
r9 (<i>fixed</i>)	1,487	0.333	0.293	0.414	0.428	0.547
r10 (<i>fixed</i>)	8,582	0.752	0.259	0.393	0.406	0.494
adaptive (<i>ours</i>)	1,494	0.297	0.286	0.424	0.445	0.548

[†]r7 defines a trivial 46-class prediction task, so its low val loss is not comparable across resolutions; the retrieval columns is a more fair indicator.

The density-adaptive vocabulary achieves the strongest overall retrieval profile, with the best comparable validation loss, MRR, NDCG@5, and Spearman correlation. We note that fixed r9 is negligibly higher on HR@1 (0.293 vs. 0.286) — a difference of seven queries in the 1k-query bank. Since HR@1 depends on the single exact-DTW nearest neighbor, this suggests that uniform r9 can occasionally better recover the exact top match in dense regions. However, the adaptive tokenizer ranks the broader neighborhood more consistently, as reflected by its stronger MRR, NDCG@5, and Spearman scores. Coarser resolutions (r7, r8) lack spatial precision, while finer resolution (r10) fragments the vocabulary and weakens statistical support per cell. The adaptive scheme resolves this tradeoff by allocating fine cells where data density warrants them, a capacity no single fixed resolution can match.

4.6.2 Cross-Attention Fusion Between Factorized Channels

Our architecture factorizes trajectory representation into a geometric channel and a kinematic channel, coupled by cross-attention fusion layers. We test whether each component of this design is necessary by evaluating four architectural variants across all four downstream tasks.

Table 6: Architectural ablation across all four downstream tasks. Similarity reports HR@1; classification reports macro-F1; ETA and TTE report MAE in seconds (lower is better). Best results in **bold** and second best results are underlined.

Variant	Similarity \uparrow	Classification \uparrow	ETA \downarrow	TTE \downarrow
Geometric (only)	<u>0.286</u>	<u>0.773</u>	44.44	87.52
Kinematic (only)	0.028	0.632	<u>43.71</u>	91.94
Both (no fusion)	0.251	0.729	46.33	<u>53.09</u>
TrajTok (ours)	0.297	0.783	40.21	47.10

The four variants in Table 6 expose a clear specialization–generalization tradeoff. Each single-channel ablation dominates the tasks aligned with its inductive bias: the geometric-only encoder has advantage on similarity (0.286 HR@1) and classification (0.773 macro-F1), both driven by *where* a trajectory goes, while the kinematic-only encoder wins on prefix ETA (43.71 s MAE), which depends on *how* it moves. Removing either channel is catastrophic on the complementary regime—kinematic-only collapses on similarity to near-chance (0.028 HR@1), and both single-channel variants lose 40+ s of MAE on full-trajectory TTE, a task that jointly requires spatial context (route) and motion dynamics (pace). The factorized-no-fusion variant shows that merely exposing the task head to both streams is insufficient: it underperforms each specialist on its specialty and still trails the full model on TTE by nearly 6 s, indicating that isolated channels fail to exploit their complementarity. Cross-attention fusion is what closes this gap. Full TrajTok finishes the best on every specialist task and decisively

wins on TTE (47.10 s), the one task whose information requirement spans both regimes. This is the profile we aim for in a general-purpose trajectory encoder: near or surpass specialist quality on each single-regime task, and strict improvement wherever the two regimes must be combined.

4.6.3 Pretraining Recipe

Finally, we examine how pretraining hyperparameters affect downstream transfer. Table 7 tries three mask ratio at matched 60k steps and additionally reports a 120k continuation of our main configuration.

Table 7: Pretraining ablation. Mask ratio is swept at 60k steps; the last row extends the chosen recipe to 120k steps. Validation loss is computed on held-out pretraining data; retrieval metrics are zero-shot DTW similarity on the Porto 1k/10k bank. Best 60k result in **bold**. The 120k row shows that extending pretraining continues to lower validation loss but *regresses* on every retrieval metric, consistent with our finding that pretraining loss alone is not a sufficient model-selection signal.

Recipe	Mask ratio	Training Budget	Val loss ↓	HR@1 ↑	HR@10 ↑	MRR ↑	NDCG@10 ↑
Mild masking	0.25	60k	0.095	0.296	0.696	0.428	0.455
Strong masking	0.35	60k	0.098	0.308	0.689	0.437	0.459
More Budget	0.30	120k	0.073	0.257	0.624	0.377	0.410
<i>Ours</i>	0.30	60k	0.098	0.351	0.781	0.503	0.521

Mask ratio has a clear sweet spot. Within the 60k comparison, mask ratio 0.30 yields the strongest downstream retrieval, outperforming both milder (0.25) and stronger (0.35) corruption. Too little masking produces a weak self-supervised signal; too much destroys the contextual structure needed for successful prediction. Our current setting balances these forces.

Pretraining loss is not a *free* signal. Extending the main recipe from 60k to 120k steps reduces validation loss by 25% (0.098 → 0.073), yet zero-shot retrieval *degrades* sharply from 0.351 to 0.257. This discrepancy points to a pretraining–transfer mismatch: lower masked-token loss does not necessarily imply a more transferable trajectory representation. Appendix C.4 provides additional analysis of this objective–transfer gap.

5 Limitations

All of our experiments are conducted on the Porto taxi dataset, which is a commonly used benchmark in trajectory representation learning and supports direct comparison with prior work. It would be interesting to continue exploring: i) transfer learning capability to other dataset with minimal or zero finetuning; ii) a larger scale of pretraining with multiple cities and trajectories with more variety. So far we have verified our learned trajectory representations on two different domains across four downstream applications; we believe it is possible to include more tasks in the future to extend implications beyond what we have covered. Finally, TrajTok relies solely on raw GPS signals; a promising direction is to enrich the spatial tokens with lightweight geographic priors (e.g., map and road-network features) directly at the token level, without reverting to costly map-matching preprocessing.

6 Conclusion

We presented TrajTok, a trajectory representation learning framework that converts raw, noisy GPS traces into density-adaptive multi-resolution spatial tokens and learns transferable representations through a factorized transformer encoder with geometric–kinematic specialization, cross-attention fusion, and simple masked pretraining. Across four downstream applications spanning both geometry-dominated and motion-sensitive settings, a single frozen pretrained encoder with lightweight task heads achieved strong transfer performance, outperforming or matching specialized prior methods on trajectory similarity search, call-type classification, prefix-based ETA prediction, and full-trajectory travel-time regression. Our ablations further showed that adaptive tokenization, factorized dual-channel modeling, and careful pretraining design each contribute materially to downstream generalization. Overall, these results suggest that learned multi-resolution spatial tokenization, combined

with a simple yet effective masked objective, is a promising recipe for general-purpose trajectory foundation models, and motivate future work on scaling to broader geographies, longer trajectories, and more diverse mobility tasks.

References

- [1] Serina Chang, Emma Pierson, Pang Wei Koh, Jaline Gerardin, Beth Redbird, David Grusky, and Jure Leskovec. Mobility network models of covid-19 explain inequities and inform reopening. *Nature*, 589(7840):82–87, 2021.
- [2] Yanchuan Chang, Jianzhong Qi, Yuxuan Liang, and Egemen Tanin. Contrastive trajectory similarity learning with dual-feature attention. In *Proceedings of the 39th IEEE International Conference on Data Engineering (ICDE)*. IEEE, 2023. doi: 10.1109/ICDE55515.2023.00119.
- [3] Huanran Chen, Huaqing Zhang, Xiao Li, Yinpeng Dong, Ke Shen, and Jun Zhu. Nexus: Same pretraining loss, better downstream generalization via common minima, 2026. URL <https://arxiv.org/abs/2604.09258>. Direct support: the paper reports significantly better downstream performance despite achieving the same pretraining loss, challenging reliance on pretraining loss as the sole evaluation proxy.
- [4] Zhen Chen, Dalin Zhang, Shanshan Feng, Kaixuan Chen, Lisi Chen, Peng Han, and Shuo Shang. KGTS: Contrastive trajectory similarity learning over prompt knowledge graph embedding. In *Proceedings of the 38th AAAI Conference on Artificial Intelligence (AAAI)*. AAAI Press, 2024. doi: 10.1609/aaai.v38i8.28672.
- [5] Liwei Deng, Yan Zhao, Zidan Wang, Hao Fan, and Kai Zheng. Efficient trajectory similarity computation with contrastive learning. In *Proceedings of the 31st ACM International Conference on Information & Knowledge Management (CIKM)*, pages 229–239. ACM, 2022. doi: 10.1145/3511808.3557308.
- [6] Yanyan Fan, Ye Yuan, Guoliang Lv, Hao Chen, Jian Li, and Feifei Liu. MetaER-TTE: An adaptive meta-learning model for en route travel time estimation. In *Proceedings of the Thirty-First International Joint Conference on Artificial Intelligence*, pages 1806–1812, 2022. doi: 10.24963/ijcai.2022/251.
- [7] Xiaomin Fang, Jizhou Huang, Fan Wang, Lingke Zeng, Haijin Liang, and Haifeng Wang. ConSTGAT: Contextual spatial-temporal graph attention network for travel time estimation at baidu maps. In *Proceedings of the 26th ACM SIGKDD International Conference on Knowledge Discovery and Data Mining*, pages 2697–2705, 2020. doi: 10.1145/3394486.3403316.
- [8] Xiaomin Fang, Jizhou Huang, Fan Wang, Lihang Liu, Yibo Sun, and Haifeng Wang. SSML: Self-supervised meta-learner for en route travel time estimation at baidu maps. In *Proceedings of the 27th ACM SIGKDD Conference on Knowledge Discovery and Data Mining*, pages 2840–2848, 2021. doi: 10.1145/3447548.3467109.
- [9] Chelsea Finn, Pieter Abbeel, and Sergey Levine. Model-agnostic meta-learning for fast adaptation of deep networks. In *Proceedings of the 34th International Conference on Machine Learning*, pages 1126–1135, 2017.
- [10] Kun Fu, Fanlin Meng, Jieping Ye, and Zheng Wang. CompactETA: A fast inference system for travel time prediction. In *Proceedings of the 26th ACM SIGKDD International Conference on Knowledge Discovery and Data Mining*, pages 3337–3345, 2020. doi: 10.1145/3394486.3403387.
- [11] Jiawei Jiang, Dayan Pan, Houxing Ren, Xiaohan Jiang, Chao Li, and Jingyuan Wang. Self-supervised trajectory representation learning with temporal regularities and travel semantics. In *2023 IEEE 39th international conference on data engineering (ICDE)*, pages 843–855. IEEE, 2023.
- [12] Konstantin Klemmer, Esther Rolf, Caleb Robinson, Lester Mackey, and Marc Rußwurm. Satclip: Global, general-purpose location embeddings with satellite imagery. In *Proceedings of the AAAI Conference on Artificial Intelligence*, volume 39, pages 4347–4355, 2025.

- [13] Xiucheng Li, Kaiqi Zhao, Gao Cong, Christian S. Jensen, and Wei Wei. Deep representation learning for trajectory similarity computation. In *Proceedings of the 34th IEEE International Conference on Data Engineering (ICDE)*, pages 617–628. IEEE, 2018.
- [14] Yan Lin, Huaiyu Wan, Shengnan Guo, Jilin Hu, Christian S. Jensen, and Youfang Lin. Pre-training general trajectory embeddings with maximum multi-view entropy coding. *IEEE Transactions on Knowledge and Data Engineering*, 2023. doi: 10.48550/arXiv.2207.14539.
- [15] Hao Long, Silin Zhou, Lisi Chen, and Shuo Shang. Region-point joint representation for effective trajectory similarity learning. *Proceedings of the AAAI Conference on Artificial Intelligence*, 40(18):15439–15447, Mar. 2026. doi: 10.1609/aaai.v40i18.38571. URL <https://ojs.aaai.org/index.php/AAAI/article/view/38571>.
- [16] Zhipeng Ma, Zheyang Tu, Xinhai Chen, Yan Zhang, Deguo Xia, Guyue Zhou, Yilun Chen, Yu Zheng, and Jiangtao Gong. More than routing: Joint gps and route modeling for refine trajectory representation learning. In *Proceedings of the ACM Web Conference 2024*, pages 3064–3075, 2024.
- [17] Gengchen Mai, Krzysztof Janowicz, Bo Yan, Rui Zhu, Ling Cai, and Ni Lao. Multi-scale representation learning for spatial feature distributions using grid cells. *arXiv preprint arXiv:2003.00824*, 2020.
- [18] Gengchen Mai, Krzysztof Janowicz, Bo Yan, Rui Zhu, Ling Cai, and Ni Lao. Multi-scale representation learning for spatial feature distributions using grid cells. In *8th International Conference on Learning Representations, ICLR 2020*, 2020.
- [19] Alameen Najjar. Towards a foundation model for trajectory intelligence. In *2023 IEEE International Conference on Data Mining Workshops (ICDMW)*, pages 832–835. IEEE, 2023.
- [20] Stefan Schestakov and Simon Gottschalk. Trajectory representation learning on road networks and grids with spatio-temporal dynamics. *arXiv preprint arXiv:2411.14014*, 2024.
- [21] Jianlin Su, Murtadha Ahmed, Yu Lu, Shengfeng Pan, Wen Bo, and Yunfeng Liu. Roformer: Enhanced transformer with rotary position embedding. *Neurocomputing*, 568:127063, 2024.
- [22] Uber Technologies. H3: A Hexagonal Hierarchical Geospatial Indexing System (version 4). <https://h3geo.org/>, 2022. Accessed: April 22, 2026.
- [23] Ashish Vaswani, Noam Shazeer, Niki Parmar, Jakob Uszkoreit, Llion Jones, Aidan N Gomez, Łukasz Kaiser, and Illia Polosukhin. Attention is all you need. *Advances in neural information processing systems*, 30, 2017.
- [24] Dong Wang, Junbo Zhang, Wei Cao, Jian Li, and Yu Zheng. When will you arrive? estimating travel time based on deep neural networks. In *Proceedings of the Thirty-Second AAAI Conference on Artificial Intelligence*, pages 2500–2507, 2018.
- [25] Zhe Xu, Zhixin Li, Qingwen Guan, Dingshui Zhang, Qiang Li, Junxiao Nan, Chunyang Liu, Wei Bian, and Jieping Ye. Large-scale order dispatch in on-demand ride-hailing platforms: A learning and planning approach. In *Proceedings of the 24th ACM SIGKDD international conference on knowledge discovery & data mining*, pages 905–913, 2018.
- [26] Chen Yang, Junzhuo Li, Xinyao Niu, Xinrun Du, Songyang Gao, Haoran Zhang, Zhaoliang Chen, Xingwei Qu, Ruibin Yuan, Yizhi Li, Jiaheng Liu, Stephen W. Huang, Shawn Yue, and Ge Zhang. The fine line: Navigating large language model pretraining with down-streaming capability analysis, 2024. URL <https://arxiv.org/abs/2404.01204>. Direct support: the abstract explicitly states that pretraining-loss-based scaling focuses on compression on training data and can be inconsistent with improvements on downstream tasks.
- [27] Chuang Yang, Renhe Jiang, Xiaohang Xu, Chuan Xiao, and Kaoru Sezaki. SIMformer: Single-layer vanilla transformer can learn free-space trajectory similarity. *Proceedings of the VLDB Endowment*, 2025. doi: 10.14778/3705829.3705853.

- [28] Sean Bin Yang, Chenjuan Guo, Jilin Hu, Jian Tang, and Bin Yang. Unsupervised path representation learning with curriculum negative sampling. *arXiv preprint arXiv:2106.09373*, 2021.
- [29] Di Yao, Chao Zhang, Zhihua Zhu, Qin Hu, Zheng Wang, Jianhui Huang, and Jingping Bi. Learning deep representation for trajectory clustering. *Expert Systems*, 35(2):e12252, 2018. doi: <https://doi.org/10.1111/exsy.12252>. URL <https://onlinelibrary.wiley.com/doi/abs/10.1111/exsy.12252>. e12252 10.1111/exsy.12252.
- [30] Di Yao, Chao Zhang, Zhihua Zhu, Jianhui Hu, and Jingping Bi. Computing trajectory similarity in linear time: A generic seed-guided neural metric learning approach. In *Proceedings of the 35th IEEE International Conference on Data Engineering (ICDE)*, pages 1358–1369. IEEE, 2019. doi: 10.1109/ICDE.2019.00123.
- [31] Di Yao, Haonan Hu, Lun Du, Gao Cong, Shi Han, and Jingping Bi. TrajGAT: A graph-based long-term dependency modeling approach for trajectory similarity computation. In *Proceedings of the 28th ACM SIGKDD Conference on Knowledge Discovery and Data Mining (KDD)*, pages 2275–2285. ACM, 2022. doi: 10.1145/3534678.3539358.
- [32] Yu Zheng, Licia Capra, Ouri Wolfson, and Hai Yang. Urban computing: concepts, methodologies, and applications. *ACM Transactions on Intelligent Systems and Technology (TIST)*, 5(3): 1–55, 2014.
- [33] Yuanshao Zhu, James Jianqiao Yu, Xiangyu Zhao, Xun Zhou, Liang Han, Xuetao Wei, and Yuxuan Liang. Unitraj: Learning a universal trajectory foundation model from billion-scale worldwide traces. In *The Thirty-ninth Annual Conference on Neural Information Processing Systems*, 2025.

A Algorithm: Density-Adaptive Vocabulary Construction

Algorithm 1 Density-Adaptive Vocabulary Construction

Require: point stream \mathcal{P} ; base resolution r_{\min} ; max resolution r_{\max} ; capacity threshold C

Ensure: vocabulary \mathcal{V} of (cell_id, resolution) pairs

```

1: for all  $p \in \mathcal{P}$  do
2:    $c \leftarrow \text{H3CELL}(\text{LATLON}(p), r_{\min})$ 
3:    $\text{count}[c] += 1$ 
4: end for
5:  $Q \leftarrow \{(c, r_{\min}, \text{count}[c]) : \text{count}[c] > C\}$ 
6:  $\mathcal{V} \leftarrow \{c : \text{count}[c] \leq C\}$ 
7: while  $Q \neq \emptyset$  do
8:    $(c, r, S) \leftarrow \text{POP}(Q)$ 
9:   if  $|S| > C$  and  $r < r_{\max}$  then
10:    for all  $c' \in \text{CHILDREN}(c, r + 1)$  do
11:       $S' \leftarrow \{p \in S : \text{H3CELL}(p, r + 1) = c'\}$ 
12:      push  $(c', r + 1, S')$  into  $Q$ 
13:    end for
14:   else
15:      $\mathcal{V} \leftarrow \mathcal{V} \cup \{c\}$ 
16:   end if
17: end while
18: return  $\mathcal{V}$ 

```

B Implementation Details

B.1 Experiment Setup

Dataset. We use the Porto taxi dataset (1,710,670 trips). After dropping incomplete data points and points outside the reasonable bounding box $[41.100, 41.220] \times [-8.700, -8.530]$, a deterministic 60/20/20 hash-based split yields 885,055 / 294,909 / 294,367 train/validation/test trajectories.

Spacial Vocabulary. Our adaptive vocabulary uses base H3 resolution 6, maximum resolution 9, and capacity 1,000 data points, yielding 1,494 cells. We visualize the vocabulary in Figure 2.

Model. The factorized encoder has 144M parameters: $d_{\text{model}}=512$, 8 heads, 16 total layers with 4 cross-attention fusion layers, $\text{max_seq_len}=192$, and operates on raw token streams. Since each attention head has dimension 64, we allocate (20, 20, 24) rotated dimensions to latitude, longitude, and time. Relative latitude and longitude are multiplied by 10^4 before forming rotary angles.

Hyperparameters. Factorized masked objective (§3.5) with mask ratio 0.3, run-aware span masking ($\ell=6$), AdamW ($\text{lr}=10^{-4}$, $\text{wd}=0.01$), cosine decay with 20% warmup, bf16, effective batch size 256, for 60k steps. Motion loss weights $\beta_{\text{speed}}=\beta_{\text{heading}}=1.0$. For hyperparameter ablations, please see §4.6.

Computing Resources. All experiments ran on a single GPU (NVIDIA RTX 6000 Ada Generation cards with 48 GiB VRAM). Pretraining the main TrajTok dual-stream model takes roughly 1.5-2 hours per run; downstream finetuning for similarity, classification, ETA, and TTE completes in 30–60 minutes per run with the encoder frozen.

B.2 Downstream Adapter Configurations

Throughout §4.2–§4.5 the pretrained TrajTok encoder is frozen and only a lightweight, task-specific adapter is trained on top. Below we detail the adapter architecture, training data, and optimization settings used for each benchmark.

Trajectory Similarity Search (§4.2). The retrieval head is an attentive pooling layer followed by a linear projection, applied to the frozen encoder output and L2-normalized for cosine-similarity ranking. It is trained on a separate train bank of 2,048 queries against 8,192 corpus trajectories, disjoint from the evaluation bank (1,000 queries against a 10,000-trajectory corpus). The objective combines InfoNCE contrastive loss with a rank-distillation term against DTW ground truth, with early stopping on validation HR@1.

Trajectory Classification (§4.3). The call-type classifier concatenates an attentive-pooled trajectory embedding with a compact departure-context branch consisting of the start token, start location, and a 32-dim origin-time interaction feature. Training uses AdamW ($\text{lr}=3 \times 10^{-3}$, $\text{wd}=0.05$) with batch size 4,096.

ETA from Prefixes (§4.4). An attentive pooling layer conditioned on the destination token aggregates the prefix-trajectory representation, which is then mapped to the remaining travel time by a lightweight regressor. Training uses a randomized-prefix regime in which the observed prefix ratio is sampled per example as $|\text{prefix}| \sim U[40\%, 60\%]$ so that the head is exposed to a wide range of completion ratios.

Full-Trajectory Travel-Time Regression (§4.5). The full-trip regressor mirrors the ETA adapter (attentive pooling followed by a lightweight regressor) but consumes the entire observed trajectory and omits prefix sampling.

B.3 Attention

This subsection gives formal definitions of the self-attention and cross-attention operations referenced in §3.4 and equations (3)–(6) of the main text. Both are instantiated as multi-head scaled dot-product attention [23] with rotary position embeddings (RoPE) [21] applied to the per-head query and key projections.

Scaled dot-product attention. Given queries $Q \in \mathbb{R}^{L_q \times d_h}$, keys $K \in \mathbb{R}^{L_k \times d_h}$, and values $V \in \mathbb{R}^{L_v \times d_h}$, scaled dot-product attention is defined as

$$\text{Attn}(Q, K, V) = \text{softmax}\left(\frac{QK^\top}{\sqrt{d_h}}\right)V. \quad (6)$$

Multi-head attention concatenates H parallel heads of dimension $d_h = d/H$:

$$\text{MHA}(X_Q, X_K, X_V; \mathbf{P}_Q, \mathbf{P}_K) = \text{Concat}(\text{head}_1, \dots, \text{head}_H)W^O, \quad (7)$$

with

$$\text{head}_h = \text{Attn}\left(\mathcal{R}\left(X_Q W_h^Q; \mathbf{P}_Q\right), \mathcal{R}\left(X_K W_h^K; \mathbf{P}_K\right), X_V W_h^V\right), \quad (8)$$

where $W_h^Q, W_h^K, W_h^V \in \mathbb{R}^{d \times d_h}$, $W^O \in \mathbb{R}^{d \times d}$, and $\mathcal{R}(\cdot; \mathbf{p})$ denotes the RoPE rotation conditioned on positional coordinates \mathbf{p} .

Rotary position embedding. For a token j in the *kinematic* channel, $\mathbf{p}_j = t_j$ is the trajectory-relative timestamp, and \mathcal{R} applies a one-dimensional temporal rotation across all d_h head dimensions. For a token in the *geometric* channel, $\mathbf{p}_j = (\phi_j, \lambda_j, t_j)$ is a three-axis spatiotemporal tuple; the head is partitioned into disjoint blocks of sizes (d_ϕ, d_λ, d_t) with $d_\phi + d_\lambda + d_t = d_h$, and each coordinate rotates its corresponding block independently. In our implementation, $d_h = 64$ and $(d_\phi, d_\lambda, d_t) = (20, 20, 24)$; relative latitudes and longitudes are multiplied by 10^4 before forming rotary angles.

Self-attention. Let $X^{(\ell)} \in \mathbb{R}^{L \times d}$ denote the hidden states of a single channel at layer ℓ , associated with per-token positional coordinates $\mathbf{P} = \{\mathbf{p}_j\}_{j=1}^L$. Self-attention draws queries, keys, and values from the same input:

$$\text{SelfAttn}\left(X^{(\ell)}; \mathbf{P}\right) = \text{MHA}\left(X^{(\ell)}, X^{(\ell)}, X^{(\ell)}; \mathbf{P}, \mathbf{P}\right). \quad (9)$$

The two streams differ only in the choice of \mathbf{P} : $\text{SelfAttn}_{\text{geo}}$ uses the spatiotemporal tuple $\mathbf{p}_j = (\phi_j, \lambda_j, t_j)$, while $\text{SelfAttn}_{\text{kin}}$ uses the temporal coordinate $\mathbf{p}_j = t_j$ alone.

Cross-attention. In a fusion block, each stream queries the other. Given two channels $X^{(\ell)}, Y^{(\ell)} \in \mathbb{R}^{L \times d}$ over the same token positions, cross-attention on X with context Y is

$$\text{CrossAttn}\left(X^{(\ell)}, Y^{(\ell)}; \mathbf{P}\right) = \text{MHA}\left(X^{(\ell)}, Y^{(\ell)}, Y^{(\ell)}; \mathbf{P}, \mathbf{P}\right), \quad (10)$$

i.e. queries are projected from X while keys and values are projected from Y . Because fusion layers align geometric and kinematic tokens in a shared spatiotemporal frame, both $\text{CrossAttn}_{\text{geo}}$ and $\text{CrossAttn}_{\text{kin}}$ use the spatiotemporal coordinates $\mathbf{p}_j = (\phi_j, \lambda_j, t_j)$.

Let $G^{(\ell)}$ and $K^{(\ell)}$ denote the geometric and kinematic hidden states at layer ℓ . We have:

$$G^{(\ell+1)} = \text{CrossAttn}\left(\tilde{G}^{(\ell)}, K^{(\ell)}; \mathbf{P}\right), \quad (11)$$

$$K^{(\ell+1)} = \text{CrossAttn}\left(\tilde{K}^{(\ell)}, G^{(\ell)}; \mathbf{P}\right). \quad (12)$$

Block structure. Every attention sublayer is wrapped in a pre-norm residual block followed by a two-layer GeGLU MLP, consistent with Figure 1 (Middle):

$$X' = X + \text{SelfAttn}(\text{LN}(X); \mathbf{P}), \quad (13)$$

$$X'' = X' + \text{MLP}(\text{LN}(X')), \quad (14)$$

with analogous pre-norm wrapping for the cross-attention sublayers in the fusion blocks.

B.4 ETA Baselines

For *Hoch-style gradient-boosted regressor* (LightGBM, Huber loss, log1p target, up to 3000 trees with early stopping on validation MAE), we manually derived the following features: calendar context (weekday, hour, sinusoidal time-of-day), prefix shape (length, duration, cumulative and

straight-line distance), current state (latitude, longitude, speed, heading, distance-to-city-center), recent-window means over the last five points, and destination conditioning (destination coordinates, Haversine from current point to destination, bearing to destination). This follows the spirit of the ECML/PKDD 2015 Porto taxi-ETA challenge winner, extended with the destination cues that match our protocol.

For *prefix-cell* \times *destination-cell* *kNN*, we index every training prefix by the pair of H3 cells at resolution 9 covering its prefix-last point and its destination, take a $k=10$ mean of matching remaining-time targets, and fall back through H3-r8, H3-r7, destination-cell-only, and global-mean when the exact bucket is sparse. On our test set, 95.4% of queries resolve at exact H3-r9, indicating that the memorization baseline is genuinely exercised and not dominated by fallbacks.

C Supplementary Ablations

This appendix reports additional ablation studies that are included for completeness. These studies cover (i) masking-strategy variants, (ii) a deduplication control, and (iii) a classification-head design study. Unless otherwise noted, all experiments use the same dual-stream encoder, pretraining objective, and evaluation protocols as the main paper.

C.1 Masking Strategy: Naive vs. Run-Aware Span Masking

Raw token streams often contain repeated-cell runs, which can make naive span masking degenerate. In particular, when a masked span covers only the interior of a constant-cell block, the missing tokens are trivially recoverable from the visible endpoints. Our main recipe therefore uses run-aware span masking, which keeps the masked objectives unchanged but avoids this shortcut in the corruption process.

For a length- L sequence, we set the mask budget to $\lfloor \rho L \rfloor$ and sample candidate span lengths uniformly from $\{\ell - 1, \ell, \ell + 1\}$ around the average span length ℓ . A candidate span is rejected if both endpoints lie strictly inside the same repeated-cell run, meaning that the span would mask only the interior of one constant-cell block. After rejection sampling, any remaining budget is filled first from non-interior tokens and only then, if necessary, from arbitrary valid tokens. Table 8 compares this run-aware strategy with naive span masking under matched 12k-step budgets.

Table 8: Masking strategy comparison at matched 12k training steps. Both rows use raw token streams, mask ratio 0.30, and identical encoder configurations.

Masking strategy	Val loss \downarrow	HR@1 \uparrow	MRR \uparrow	Spearman \uparrow
Naive	0.276	0.286	0.424	0.524
Run-aware (ours)	0.297	0.308	0.442	0.548

The two strategies show clear distinctions on pretraining loss score and downstream performance: while naive span masking does provide a lower loss in general, the representations learned are outperformed by our run-aware strategy, which indicates that run-aware masking prevent the model from taking the shortcuts by simply copying surrounding tokens and incentivize it to actually learn from high level geometric features.

C.2 Deduplicated vs. Raw Token Sequences

Our main backbone pretrains on complete token sequence, which preserve dwell patterns and repeated-cell motion cues at the cost of longer sequences. We also tried another de-duplicate design which collapse consecutive repeated cells. Table 9 reports the deduplicated control for transparency.

C.3 Call-Type Classification Head Design

The main paper reports call-type classification results using our best head configuration: attentive-pooled encoder features concatenated with a compact departure-context branch (start token, start location, and a 32-dim origin-time interaction). Here we report variants of this head, holding the

Table 9: Deduplicated vs. raw token streams. The two configurations differ in both sequence length and masking strategy, so this comparison is not fully matched.

Configuration	Val loss ↓	HR@1 ↑	MRR ↑
Dedup	0.098	0.309	0.459
Ours	0.047	0.351	0.588

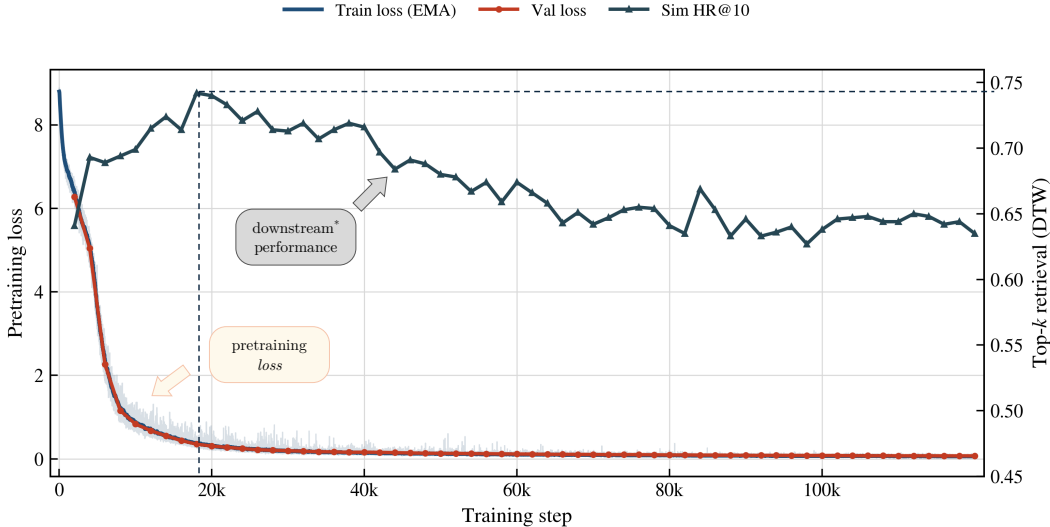


Figure 3: Mismatch between pretraining optimization and downstream utility. Although both training and validation pretraining losses decrease monotonically, downstream retrieval performance (Sim HR@10) peaks early and then gradually declines, indicating that lower pretraining loss does not necessarily yield better transfer performance.

frozen encoder fixed. This ablation studies the *task head* rather than the encoder, and is included to document design decisions in the downstream evaluation protocol.

Table 10: Call-type classification head ablation. All rows use the same frozen TrajTok encoder.

Head variant	Test accuracy ↑	Test macro-F1 ↑
Departure context + large origin-time branch	0.740	0.692
Departure context only	0.804	0.767
Departure context + compact origin-time branch (main)	0.811	0.773

A large origin-time interaction branch over-parameterizes the head and degrades performance, while omitting origin-time context entirely sacrifices useful temporal signal. The compact 32-dim branch used in our main configuration balances these extremes. These differences reflect task-head design choices and do not affect the frozen encoder representation itself.

C.4 Pretraining Recipe

During pretraining, although the training loss and validation loss both decrease steadily, the downstream performance (we use zero-shot similar trajectory search without finetuning as an indicator for simplicity), on each checkpoint, is not decreasing monotonically (see Figure 3). We believe this pretraining-benchmark mismatch signals a deeper alignment research problem which is beyond our scope and require further study [26, 3].

D Broader Impacts

TrajTok is foundational research on representation learning for GPS trajectories, with positive potential applications in urban planning, public transit optimization, traffic management, ride-hailing efficiency, and epidemic modeling, all of which can improve mobility services and public health outcomes. However, we acknowledge that any technology that produces transferable representations of human movement carries privacy and surveillance risks: trajectory embeddings can facilitate re-identification of individuals from sparse location traces, enable behavioral profiling, and lower the cost of large-scale mobility tracking if applied to non-consented data. These risks apply whether the model is functioning correctly (intended downstream tasks may still aggregate sensitive mobility patterns), produces incorrect outputs (misclassification could propagate into downstream decisions affecting individuals or groups, e.g., in dispatch or pricing systems), or is misused (adversaries repurposing pretrained encoders for tracking or stalking). All experiments in this paper use the publicly released Porto taxi dataset, which contains anonymized vehicle (not individual user) trajectories collected and released for research, and we do not collect new mobility data. To mitigate misuse, we recommend that practitioners building on TrajTok apply standard privacy safeguards — including k-anonymity or differential privacy on training data, restricting access to pretrained checkpoints trained on sensitive corpora, and avoiding fine-grained re-identification tasks — and we will document these considerations in any code or model release.